

Estimating Target Doppler in Unsynchronized Multistatic ISAC Deployments with Mobile Nodes

Zaman Bhalli
University of Padova
Padova, Italy
zaman.bhalli@unipd.it

Michele Rossi
University of Padova
Padova, Italy
michele.rossi@unipd.it

Joerg Widmer
IMDEA Networks Institute
Madrid, Spain
joerg.widmer@networks.imdea.org

Marco Canil*
IMDEA Networks Institute
Madrid, Spain
marco.canil@networks.imdea.org

Abstract—Integrated Sensing And Communication (ISAC) is recognized as a key enabler for future 6th Generation (6G) networks, combining communication capabilities with pervasive sensing. In such systems, the estimation of the Doppler shift plays a crucial role for target characterization. However, typical real-world ISAC scenarios largely involve bistatic or multistatic configurations and mobile ISAC nodes. Under these conditions, Doppler estimation becomes particularly challenging, as clock asynchrony between the Transmitter (TX) and the Receivers (RXs), combined with their mobility, introduces additional Doppler components and phase offsets that distort or disrupt the target-induced frequency shift. Existing works have considered these challenges separately or relied on external reference reflectors.

In this paper, we present the first method to estimate the Doppler frequency of a target with mobile and asynchronous ISAC nodes in a multistatic configuration, considering the case of a mobile TX and multiple static RXs, and without leveraging any external reflector. By leveraging the invariance of the phase offsets across multipath components and exploiting geometrical relationships, we show that the problem is solvable if at least 4 RXs are present. We evaluate the proposed solution through numerical simulations in various scenarios, showing that it is a valid approach for estimating target Doppler shifts in unsynchronized multistatic ISAC deployments with mobile nodes.

Index Terms—ISAC, Doppler, 6G, mobility, multistatic

I. INTRODUCTION

Considered as one of the cornerstones for the 6th Generation of wireless networks [1], ISAC is expected to become an essential component of future wireless infrastructures. Seeking to embed sensing functionalities directly into communication

systems, the promise is to enable a pervasive radio-based sensing fabric that extends over the whole communication network. In ISAC applications, accurate Doppler shift estimation plays a crucial role in target characterization [2] and in determining target motion [3], making it a fundamental sensing feature. In the ISAC vision, the sensing functionality will predominantly rely on bistatic configurations, i.e., with physically separated TX and RX, as ISAC nodes are expected to consist of a combination of gNodeBs (gNBs) and User Equipments (UEs). In this context, the estimation of the Doppler shift poses several additional challenges compared to monostatic cases. Due to the unsynchronized clocks of the TX and RX, the received signal is affected by Timing Offset (TO), Carrier Frequency Offset (CFO), and Phase Offset (PO), which act as disturbance terms and hinder the reconstruction of the target's Doppler. Moreover, the motion of one or both ISAC nodes introduces an additional Doppler component that dynamically combines with that of the target in a non-trivial manner.

Current studies mainly address the challenges arising from clock asynchronies with *static* devices [3]–[6], or consider *mobile* monostatic radars, which are not affected by such issues. In [7] and [8], the authors tackle both problems at the same time, but their approach relies on the concurrent presence of Line-of-Sight (LoS) and external static reflectors, limiting the applicability in real-world scenarios.

In this work, we present a method for estimating the Doppler of a moving target using unsynchronized and mobile ISAC nodes, without relying on any external reflectors. Specifically, we consider an asynchronous multistatic configuration with one TX and multiple RXs. Both the TX and the target are moving, while the RXs remain static at fixed known locations. In the envisioned scenario, the TX corresponds to a mobile UE, while the RXs could be different RXs of a 5G New Radio (5G NR) gNB or components of a Cloud Radio Access Network (C-RAN), where coherent processing is possible [9]. Please, note that industrial implementations of C-RANs are becoming available [10]. An illustrative (but not limiting) example is that of a micro gNB [11] deployed in an urban street canyon, featuring multiple overlapping RXs with highly directional beams. Such beams can be dynamically steered and adjusted to accommodate different communication and sensing requirements. We assume that all RXs are phase-synchronized at baseband but employ separate Radio

* corresponding author.

This work was supported by the European Union's Horizon 2020 research and innovation programme under the Marie Skłodowska-Curie COFUND Doctoral Programme "UNIPhD – Eight Century Legacy of Multidisciplinary Research and Training for the Next-Generation Talents", grant agreement No. 101034319.

This publication is part of grant JDC2024-055419-I, funded by MICIU/AEI/10.13039/501100011033 and by the ESF+.

The work presented in this paper is (partially) supported by the MultiX project that has received funding from the Smart Networks and Services Joint Undertaking (SNS JU) under the European Union's Horizon Europe research and innovation programme under Grant Agreement No 101192521.

This work has been funded by project PID2022-136769NB-I00 funded by MICIU/AEI/10.13039/501100011033 / FEDER, UE.

TUCAN6-CM (TEC-2024/COM-460), funded by Comunidad de Madrid (ORDEN 5696/2024).

Frequency (RF) front ends (i.e., with separate mixers, Phase-Locked Loop (PLL), etc.). With this configuration, each RX experiences a slightly different CFO after down-conversion, due to the small hardware differences in the front ends. While this difference is usually negligible for communication, removing it is critical for sensing [4], and each RX needs to independently compensate for its own CFO. In our approach, we assume that each RX receives two paths, which appear as peaks in the estimated Channel Impulse Response (CIR): the LoS path from the moving TX and the target path. Fig. 1 represents this scenario. The proposed methodology takes as input (i) the phases of the received paths, (ii) the Angle of Arrival (AoA) of each path, and (iii) the known relative position of the RXs. Then, four steps lead to the reconstruction of the target's Doppler. First, leveraging the fact that CFO and PO are common to all propagation paths of the same receiver, the LoS path is used to remove these offsets from the phases of the target path. Second, range-related phase terms are removed by taking time-domain phase differences between consecutive time steps. Third, the geometrical relationships between the phase terms and the gNB RXs are exploited to reduce the number of independent terms. Finally, a non-linear system of equations is formulated and solved to estimate the target's Doppler. As a result of the simplifications, the system becomes solvable if at least 4 RXs are available.

The main contributions of this work are:

- 1) We present the first method to estimate the Doppler frequency of a target in a multistatic scenario with mobile and asynchronous ISAC nodes.
- 2) We consider the challenging but realistic case where each ISAC RX exhibits a different CFO and PO.
- 3) We evaluate the proposed solution through numerical simulations in various scenarios, showing that it represents a valid solution for the estimation of Doppler shifts in realistic multistatic ISAC scenarios.

The remainder of the paper is organized as follows. Section II and Section III describe the system model and the proposed methodology, respectively. Section IV presents the simulation setup along with the obtained results, while Section V provides the concluding remarks.

II. SYSTEM DESCRIPTION AND MODELING

This section presents the system architecture and model considered for our new Doppler estimation technique.

A. Reference scenario

We consider an asynchronous multistatic configuration with one TX and multiple RXs. Both the TX and the target are moving, while the RXs, indexed by $n = 1, \dots, N_{\text{rx}}$, remain static at fixed known locations. In the envisioned scenario, the TX corresponds to a mobile UE, while the RXs could be different sectors of a 5G NR gNB or components of a C-RAN, where coherent processing can be practically implemented [9], [10]. Fig. 1 provides a schematic representation of the system for the case where $N_{\text{rx}} = 4$ and the RXs are located along a straight line with equal separation. As represented in the

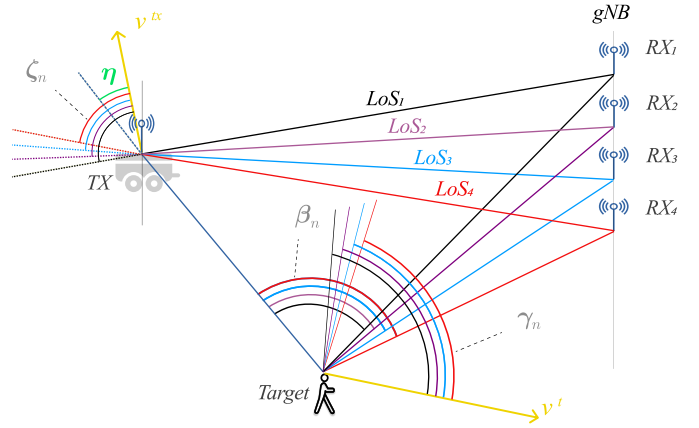


Figure 1: Geometric representation of the considered scenario with LoS and target paths.

figure, we assume each RX to receive (i) a LoS path directly from the TX, and (ii) a target path coming from the scattering of the transmitted signal off the target. The *LoS path* contains contributions from the distance and the motion of the TX and is affected by the CFO, PO, and TO of the specific TX-RX pair. The *target path*, instead, contains a combination of target- and TX-induced components and is also affected by CFO, PO, and TO.

B. Continuous-Time Channel Model

We model the continuous-time CIR at RX n , time t , and delay τ as [12]:

$$h_n(t, \tau) = e^{j\psi_{o,n}(t)} \sum_{m=1}^{M_n(t)} A_{m,n}(t) e^{j\vartheta_{m,n}(t)} \cdot \delta(\tau - \tau_{m,n}(t) - \tau_{o,n}(t)) + w_n(t, \tau), \quad (1)$$

where $\delta(\cdot)$ is the Dirac delta function, m index the $M_n(t)$ propagation paths, $A_{m,n}(t)$ embodies the complex path amplitude accounting for propagation loss, reflection and scattering phenomena, $\tau_{m,n}(t)$ denotes the instantaneous propagation delay, $\psi_{o,n}(t)$ is the PO, $\tau_{o,n}(t)$ is the TO, and $w_n(t, \tau)$ is an Additive White Gaussian Noise (AWGN) component. Phase term $\vartheta_{m,n}(t)$ comprises Doppler shifts and CFO and is expressed as [13]:

$$\vartheta_{m,n}(t) = 2\pi t \left(f_{D,m,n}^{\text{tx}}(t) + f_{D,m,n}^{\text{tgt}}(t) + f_n^{\text{c}}(t) \right), \quad (2)$$

where $f_{D,m,n}^{\text{tx}}(t)$, $f_{D,m,n}^{\text{tgt}}(t)$, and $f_n^{\text{c}}(t)$ denote the Doppler frequency of the TX, of the target, and the CFO, respectively. Let us analyze the components of Eq. (2) for the LoS and target paths. Considering the LoS path, there is no Doppler shift from the target, therefore $f_{D,m,n}^{\text{tgt}}(t) = 0$. Taking Fig. 1 as a reference and using subscripts “LoS” and “tgt” to indicate the LoS and target paths, respectively, the TX Doppler shift can be expressed as [13]:

$$f_{D,\text{LoS},n}^{\text{tx}}(t) = \frac{\|\mathbf{v}_{\text{tx}}\|}{\lambda} \cos(\zeta_n(t)), \quad (3)$$

where \mathbf{v}_{tx} is the TX velocity, $\|\cdot\|$ extracts the magnitude of a vector, $\zeta_n(t)$ is the angle between the transmitter's velocity

vector and the elongation of the line connecting the RX to the TX, and λ is the wavelength of the carrier wave. Regarding the target path, the TX Doppler is expressed as [13]:

$$f_{D,\text{tgt},n}^{\text{tx}}(t) = \frac{\|\mathbf{v}_{\text{tx}}\|}{\lambda} \cos(\eta(t)), \quad (4)$$

where $\eta(t)$ is the angle between the TX velocity vector and the elongation of the line connecting the target to the TX. The target Doppler, instead, is expressed as [13]:

$$f_{D,\text{tgt},n}^{\text{tgt}}(t) = \frac{\|\mathbf{v}_{\text{tgt}}\|}{\lambda} \cos(\gamma_n(t)) \cos(\beta_n(t)/2), \quad (5)$$

where \mathbf{v}_{tgt} is the target's velocity vector, $\beta_n(t)$ is the angle between the TX and the RX, with vertex at the target, also known as the *bistatic angle*, and $\gamma_n(t)$ is the angle between the target velocity and the bisector of the bistatic angle. Finally, both LoS and target paths are affected by the same CFO $f_n^o(t)$ which, however, only depends on the receiver n and not on the path index m .

C. Discrete-Time Measurement Model

Practical implementations of ISAC systems usually require the discretization of continuous-time signals. Under the common assumption that the channel's dynamic characteristics change negligibly throughout a short time interval T , we discretize the continuous-time CIR at RX n , discrete time k , and delay bin l , as [12]:

$$h_n[k, l] = e^{j\psi_n^o[k]} \sum_{m=1}^{M_n[k]} A_{m,n}[k] e^{j\vartheta_{m,n}[k]} \cdot \delta[l - \tau_{m,n} - \tau_{o,n}[k]] + w_n[k, l], \quad (6)$$

where the terms are the discrete counterparts of the terms defined in Eq. (1) and the discrete version of Eq. (2) is [12]:

$$\vartheta_{m,n}[k] = 2\pi kT \left(f_{D,m,n}^{\text{tx}}[k] + f_{D,m,n}^{\text{tgt}}[k] + f_n^o[k] \right). \quad (7)$$

D. Measured Phase Model

The proposed Doppler estimation technique (see Section III) primarily exploits the phases corresponding to the LoS and target paths in the CIR. We formalize the phase corresponding to the generic m -th path, at the n -th RX, at time k , as:

$$\phi_{m,n}[k] = \Psi_n^o[k] + \angle A_{m,n} + \chi_{m,n}[k] + \epsilon_{m,n}[k]. \quad (8)$$

In the formula, $\Psi_n^o[k] = \psi_n^o[k] + 2\pi kT f_n^o[k]$ summarizes the combined effect of PO and CFO, $\angle \cdot$ is the phase operator, $\chi_{m,n}[k] = 2\pi kT \left(f_{D,m,n}^{\text{tx}} + f_{D,m,n}^{\text{tgt}} \right)$ captures the contribution of the Doppler components, and $\epsilon_{m,n}[k]$ is a residual noise component. Term $\angle A_{m,n}$ indicates the phase component due to the length of the path. Considering a short-enough time window, it is reasonable to assume this value to remain constant across different time instants and we therefore drop time index k .

III. METHODOLOGY

The methodology proposed in this paper proceeds in four main stages. First, we remove the CFO and PO of each TX-RX pair, independently. Second, we perform temporal phase differentiation to eliminate the static phase terms. Third, we build a system of equations and reduce the number of unknowns by means of geometric simplifications. Finally, we estimate the remaining unknowns, including the target's Doppler, by solving a nonlinear optimization problem. Once the components of the Doppler frequency are estimated, we can compute the Doppler frequency of the target as a final result. With this procedure, we use the measurements from all the RXs to estimate the Doppler frequency of the target at *one* of the RXs. As discussed later, we found that the minimum number of RXs required for the system to be solvable is $N_{\text{rx}} = 4$.

In the following, we detail each stage of the methodology.

A. Removal of Carrier Frequency Offset and Phase Offset

As described in Section II-D, $\Psi_n^o[k]$ incorporates the phase terms due to CFO and PO. This term varies at every time step k , but, at a fixed k , is common across all multipath components received at RX n . To remove its effect, we adopt the methodology proposed in [3] and we subtract the LoS path from the target path at each RX, obtaining:

$$\Delta\phi_n[k] = \phi_{\text{tgt},n}[k] - \phi_{\text{LoS},n}[k], \quad (9)$$

where subscripts ‘‘tgt’’ and ‘‘LoS’’ indicate the target and LoS paths, respectively. By substituting the right-hand terms using Eq. (8), Eq. (9) can be rewritten as:

$$\Delta\phi_n[k] = \Delta\angle A_n + \Delta\chi_n[k] + \Delta\epsilon_n[k], \quad (10)$$

where $\Delta\angle A_n = \angle A_{\text{tgt},n} - \angle A_{\text{LoS},n}$, $\Delta\chi_n[k] = \chi_{\text{tgt},n}[k] - \chi_{\text{LoS},n}[k]$, and $\Delta\epsilon_n[k] = \epsilon_{\text{tgt},n} - \epsilon_{\text{LoS},n}$. $\Delta\chi_n[k]$ is explicitly expressed as:

$$\Delta\chi_n[k] = 2\pi kT \left(f_{D,\text{tgt},n}^{\text{tx}}[k] + f_{D,\text{tgt},n}^{\text{tgt}}[k] - f_{D,\text{LoS},n}^{\text{tx}}[k] \right). \quad (11)$$

Consequently, out of the $2N_{\text{rx}}$ phase measurements jointly extracted by the N_{rx} RXs (target and LoS path for each of them), only N_{rx} remain after the removal of PO and CFO.

B. Removal of Static Phase Terms

The step described in Section III-A eliminates the CFO and PO. However, the resulting spatially differenced phases $\Delta\phi_n[k]$ still encompass the amplitude phase terms $\Delta\angle A_n$, which depend on the length of the paths. As mentioned in Section II-D, if T is sufficiently small, $\Delta\angle A_n$ can be considered constant for two subsequent time instants. Hence, we remove it by applying a time domain phase differencing between consecutive frames. Formally,

$$\Delta\phi'_n[k] = \phi'_n[k] - \phi'_n[k-1]. \quad (12)$$

Expanding this expression using Eq. (10) yields:

$$\Delta\phi'_n[k] = \Delta\chi'_n[k] + \Delta'\epsilon_n[k], \quad (13)$$

where $\Delta\chi'_n[k] = \Delta\chi_n[k] - \Delta\chi_n[k-1]$ and $\Delta'\epsilon_n[k]$ aggregates the noise resulting from the temporal differencing operation.

In Eq. (13), the amplitude-related phase terms are removed, and only the Doppler-related components remain. By using Eq. (11), $\Delta\chi'_n[k]$ can be formulated explicitly as:

$$\Delta\chi'_n[k] = 2\pi T \left(f_{D,\text{tgt},n}^{\text{tx}}[k] + f_{D,\text{tgt},n}^{\text{tgt}}[k] - f_{D,\text{LoS},n}^{\text{tx}}[k] \right). \quad (14)$$

In Eq. (14), time difference operation reduces kT to T .

C. Geometric Simplification

In Eq. (14), the Doppler frequencies can be expanded according to Eq. (3), Eq. (4), and Eq. (5), resulting in:

$$\begin{aligned} \Delta\chi'_n = & 2\pi T \left(\frac{\|\mathbf{v}_{\text{tx}}\|}{\lambda} \cos(\eta) + \right. \\ & + \frac{\|\mathbf{v}_{\text{tgt}}\|}{\lambda} \cos(\gamma_n) \cos\left(\frac{\beta_n}{2}\right) + \\ & \left. - \frac{\|\mathbf{v}_{\text{tx}}\|}{\lambda} \cos(\zeta_n) \right), \end{aligned} \quad (15)$$

with $n = 1, \dots, N_{\text{rx}}$ and where the time index k has been dropped to improve clarity. This set of equations forms a system of N_{rx} equations in $3N_{\text{rx}} + 3$ unknowns, namely $\mathbf{v}_{\text{tx}}, \mathbf{v}_{\text{tgt}}, \eta, \gamma_n, \beta_n$, and ζ_n . $\Delta\chi'_n$, on the left-hand side, can be computed based on the measured phases.

In this shape, the system results underdetermined and cannot be solved. Therefore, in the following, we derive some geometrical simplifications that allow to reduce the number of unknowns of the system (or, equivalently, to increase the number of independent equations). In particular, the simplifications are based on the known AoAs of the received paths and on the the known relative positions of the RXs.

For simplicity, let us consider the scenario presented in Fig. 2, where $N_{\text{rx}} = 4$ and the RXs are placed along a vertical line, and let us take the RX with $n = 1$ as a reference RX for the subsequent derivations. The computations can be easily extended to arbitrary geometries. By combining the known locations of the RXs and the AoAs of the received paths, we use the n LoS paths to localize the TX, and the n target paths to localize the target. For each pair of RXs, an estimate of the target and TX locations is computed by finding the intersection point of the lines originating from the RXs and following the direction of the respective AoAs. To improve robustness, we compute such estimates for all the possible combinations of RXs pairs, and then we take their average as the final estimate. Then, the estimated locations of target and TX are used to build N_{rx} triangles with vertices at TX, the target, and the n -th RX, from which angles β_n and α are estimated. Angle α is defined as in Fig. 2. Then, we note that each angle ζ_{n+1} and γ_{n+1} can be written as a function of the preceding angles ζ_n, γ_n , respectively, as illustrated in Fig. 2. Formally,

$$\begin{cases} \zeta_{n+1} = \zeta_n - (\delta_{n+1}^{\text{tx}} - \delta_n^{\text{tx}}) \\ \gamma_{n+1} = \gamma_n - (\delta_{n+1}^{\text{tx}} - \delta_n^{\text{tx}})/2 \end{cases} \quad (16)$$

for $n = 1, \dots, N_{\text{rx}} - 1$. Here, δ_n^{tx} and δ_n^{tgt} represent the AoA

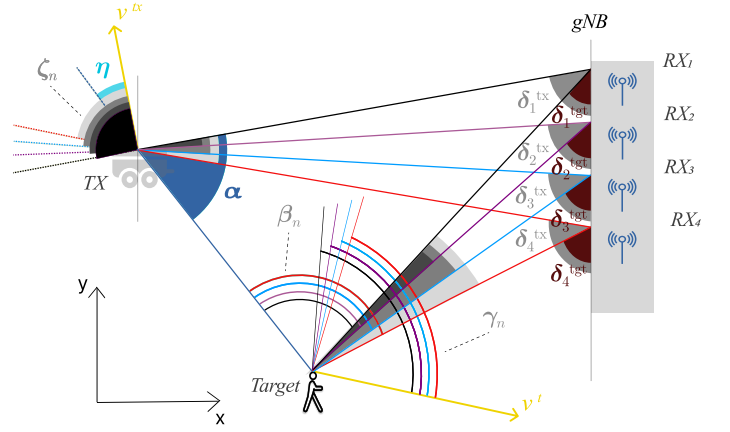


Figure 2: Representation of the paths and angles.

of the LoS and target path at the n -th RX, respectively. Note that, in Eq. (16), the only unknowns are ζ_1, γ_1 , as the others can be recursively derived from them. We also note that

$$\eta = \zeta_1 - \alpha. \quad (17)$$

Each equation in Eq. (16) allows for the reduction of $N_{\text{rx}} - 1$ unknowns, Eq. (17) allows to remove 1 more unknown (η), and the values of all the N_{rx} angles β_n were previously found through the construction of the triangles. Therefore, the system of N_{rx} equations in $3N_{\text{rx}} + 3$ unknowns of Eq. (15) is now reduced to a system with N_{rx} equations but $3N_{\text{rx}} + 3 - [2(N_{\text{rx}} - 1) + 1 + N_{\text{rx}}] = 4$ unknowns, and is solvable when $N_{\text{rx}} \geq 4$.

D. System Solution and Scalability Considerations

After the abovementioned simplifications, the system of equations in Eq. (15) only contains 4 unknowns, namely $\mathbf{v}_{\text{tx}}, \mathbf{v}_{\text{tgt}}, \zeta_1$, and γ_1 . To find them, we build a nonlinear Least Squares (LS) problem and we solve it through the Levenberg–Marquardt algorithm. To improve the quality of the estimation, after solving the system, we compute a moving average of the previous N_w solutions and use that as the final estimate. Finally, the target's Doppler frequency at one of the RXs is computed through Eq. (5). Thanks to the properties of LS and to the presented simplifications, the proposed solution directly scales to cases with more than 4 RXs, as each new RX provides an additional equation to the system, but no additional unknowns (see the end of Section III-C), thus only increasing its statistical redundancy. If $N_{\text{rx}} < 4$, the system becomes underdetermined and, therefore, does not have a unique solution. However, if one or more RXs are temporarily unavailable for a short period of time, tracking and filtering techniques can help to compensate for the missing equations.

IV. NUMERICAL RESULTS AND ANALYSIS

In this section, we describe the simulation setup and the obtained results.

A. Simulation Setup

To evaluate the performance of the proposed methodology, we generate standard-compliant 5G NR Physical Uplink Shared Channel (PUSCH) Demodulation Reference Signals

(DM-RSs) using the 5G TOOLBOX of MATLAB [14] at carrier frequency $f_c = 28$ GHz and we use them as transmitted signals in a simulator that we developed in Python. We transmit 1 DM-RS per slot. In the simulator, each target is represented by a point moving in the space with a Radar Cross-Section (RCS) $\rho \sim \text{Lognormal}(\mu_{\text{RCS}}, \sigma_{\text{RCS}}^2)$ that follows a log-normal distribution, where μ_{RCS} and σ_{RCS} are the mean and variance of $\log(\rho)$, to account for the RCS oscillations. The channel follows an AWGN model with noise spectral density of -174 dB/Hz (corresponding to a thermal noise of 290 K, and the TX uses a power of 200 mW, corresponding to the maximum allowed for a UE uplink according to 3rd Generation Partnership Project (3GPP) specifications [15]. At the RX side, a least-squares channel estimation is performed [16] using the received DM-RS symbols, and the subcarriers with no DM-RS are filled via linear interpolation. Then, CFO and PO are added independently to each RX, corresponding to the case where the RXs are phase-synchronized at baseband but have different front ends. From the CIR estimated at each RX, the phases of the LoS and target peaks are extracted and fed to our algorithm, along with the corresponding AoAs, whose error is modeled as an additive Gaussian noise $\mathcal{N}(0, \sigma_\delta^2)$. Tab. 1 summarizes the simulation parameters.

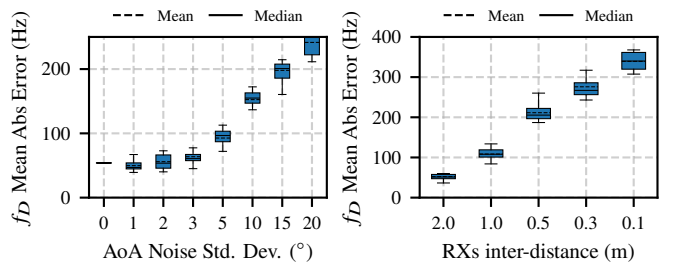
Parameter	Symbol	Value
Carrier frequency	f_c	28 GHz
Subcarrier spacing	SCS	120 kHz
Number of resource blocks	N_{RB}	52
Time slot duration	T_{slot}	125 μs
PUSCH mapping type	/	A
DM-RS configuration type	/	2
TX power	P_{TX}	200 mW
Noise spectral density	N_0	-174 dB/Hz
RCS mean parameter	μ_{RCS}	50
RCS variance parameter	σ_{RCS}^2	100

TABLE 1: SIMULATION PARAMETERS.

B. Simulation Results

We evaluate the performance of our method by computing the Mean Absolute Error (MAE) of the reconstructed Doppler as $MAE = \frac{1}{K} \sum_{k=1}^K |f_D[k] - \hat{f}_D[k]|$, where $f_D[k]$ and $\hat{f}_D[k]$ represent the true and reconstructed Doppler, respectively, and K is the total number of time steps. In the boxplots, the mean and the median are represented by a dashed and a solid line, respectively. In the evaluation, we reconstruct the Doppler at RX $n = 1$, but any RX could be equivalently selected. We remind that, in order to reconstruct the Doppler at one RX, we need to have phase and AoA data from $N_{\text{rx}} \geq 4$ receivers.

We consider a reference geometry for the simulations and then vary some of the parameters to assess their impact. The considered scenario is meant to represent a placement of the RXs loosely compatible with that of a gNB with multiple sectors, with the different RXs corresponding to the sectors, and the RXs deployed in a localized area. According to the axes represented in Fig. 2, we place the TX, target, and RXs as described in Tab. 2. We indicate with RX_n the n -th RX.



(a) Varying AoA noise. (b) Varying RXs inter-distance.

Figure 3: Target Doppler MAE versus (a) AoA noise and (b) RXs inter-distance

The velocity angle is computed counterclockwise with respect to the x axis. For the moving average, we take $N_w = 500$.

For each set of parameters, we performed 12 simulations.

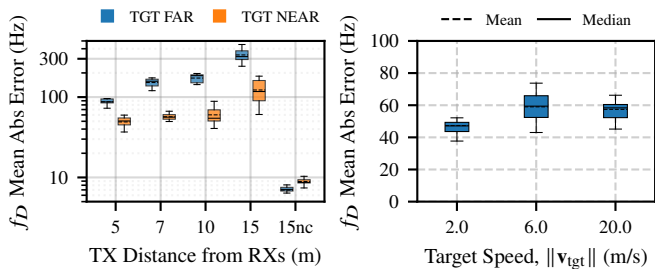
Parameter	Value	Parameter	Value
TX position	[8, 0]	AoA noise STD	2°
Target position	[12, -12]	TX velocity	4 m/s
RX ₁ position	[15, 4]	Target velocity	4 m/s
RX ₂ position	[15, 2]	TX velocity angle	225°
RX ₃ position	[15, 0]	Target velocity angle	315°
RX ₄ position	[15, -2]		

TABLE 2: REFERENCE SCENARIO PARAMETERS.

1) *Impact of AoA noise:* We start the evaluation by exploring the impact of noise on the AoAs. This is a critical aspect of the proposed solution, since many derivations rely on AoA values. We vary the AoA noise Standard Deviation (STD) as presented in Fig. 3a. As expected, the Doppler reconstruction error increases with σ_δ , with small σ_δ values (1–3°) causing a modest degradation, and larger ones (10–20°) significantly impacting the results. We consider these results satisfactory, as $MAE \leq 100$ Hz for $\sigma_\delta \leq 3^\circ$ and this level of AoA estimation accuracy is easily achievable by a RX array with 4–8 antennas or more [13]. We select $\sigma_\delta = 2^\circ$ as a realistic value and adopt it in the following evaluations.

2) *Impact of RXs inter-distance:* We study how the distance between the receivers affects the target Doppler estimate, as presented in Fig. 3b. The results show that a larger separation between the RXs, that is, a higher spatial diversity, provides better performance. As the inter-distance decreases, the paths become more similar, making it more difficult to understand the scene dynamics. Since the results drop significantly as the RXs inter-distance decreases, we pick the largest distance of 2 m and we keep it for the subsequent simulations.

3) *Impact of TX and target distance:* We explore the impact of the TX/target distance from the RXs, which allows us to characterize the operating range of the system. For the TX, we set the starting location at $y = 0$ m and we vary x as $\{10, 7, 5, 0\}$ m, corresponding to a distance from the RXs of $\{5, 7, 10, 15\}$ m, respectively. For the target, instead, we consider two starting locations: one that is near the RXs, labeled as “TGT NEAR”, and one that is far from the RXs, labeled as “TGT FAR”. The near location is set at (12, -12),



(a) Varying TX/target position. (b) Varying target speed.

Figure 4: MAE of the target Doppler as a function of (a) distance from the RXs and (b) target speed.

while the far location is set at $(8, -12)$. Since, in our scenario, we expect the distance along the x axis to be more significant than that along the y axis, the terms “near” and “far” refer to the distance along the x axis. Fig. 4a shows the results. For this particular case, to better visualize the wide dynamic range of the *MAE*, the logarithmic scale on the y axis is used. We observe that, in the “near” case, the results are satisfactory up to 10 m of distance of the TX, while in the “far” case, they are generally worse. We conclude that, with the considered placement of the RXs, the method works well only at short range, at distances compatible with those of, e.g., a narrow street. We briefly extend this examination by considering a different geometry for the placement of the RXs, to verify if and how a higher spatial diversity helps in dealing with longer distances. We place RX_1 , RX_2 , RX_3 , and RX_4 at locations $(15, -2)$, $(15, 4)$, $(-15, 4)$, and $(-15, -2)$, respectively. Basically, we keep two RXs at one side and we locate the other two at the other side, symmetrically with respect to $x = 0$, corresponding, e.g., to a deployment in a 30 m wide large street with 2 RXs per side. Then, we consider the worst case of Fig. 4a, that is, when the distance of the TX is 15 m, and we evaluate it with the new configuration. The results are labeled in Fig. 4a as “15nc”. As we can see, with higher spatial diversity, even the worst case scenario from before is tackled effectively. The downside of this geometrical configuration is that a distributed deployment of coherent RXs is much more challenging than a localized one, as that taken as a reference in this paper.

4) *Impact of target speed:* To study the impact of the target speed we consider 3 velocities, $\{2, 6, 20\}$ m/s, representative of the typical speeds of a pedestrian, a bicycle, and a car, respectively. Since we assessed that the distance along the x axis has a strong impact on the results, to isolate the effect of the speed only, for these simulations we set the angle of the velocities to 270° , that is, towards the negative direction of the y axis. The results, presented in Fig. 4b, show that our method is invariant to the speed of the target.

V. CONCLUSIONS

In this paper, we dealt with the problem of estimating the Doppler shift of a target in a multistatic scenario with a mobile TX and multiple RXs, showing that, with at least 4 RX, the problem is solvable. Simulation results show that with a

localized placement of the RXs (e.g., gNB-like), the proposed methodology works well at short range. As briefly discussed, a distributed placement of the RXs could, instead, extend the solution operating range, at the cost of an increased implementation complexity. Future works involve the optimization of the placement of the RXs and validating experimentally the proposed methodology.

REFERENCES

- [1] ITU, “Framework and overall objectives of the future development of IMT for 2030 (6G) and beyond.” 2023. [Online]. Available: <https://www.itu.int/rec/R-REC-M.2160-0-202311-I/en>
- [2] M. Canil, J. Pegoraro, and M. Rossi, “millitrace-ir: Contact tracing and temperature screening via mmwave and infrared sensing,” *IEEE Journal of Selected Topics in Signal Processing*, vol. 16, no. 2, pp. 208–223, 2022.
- [3] J. Pegoraro, J. O. Lacruz, T. Azzino, M. Mezzavilla, M. Rossi, J. Widmer, and S. Rangan, “Jump: Joint communication and sensing with unsynchronized transceivers made practical,” *IEEE Transactions on Wireless Communications*, 2024.
- [4] K. Wu, J. Pegoraro, F. Meneghello, J. A. Zhang, J. O. Lacruz, J. Widmer, F. Restuccia, M. Rossi, X. Huang, D. Zhang *et al.*, “Sensing in bistatic isac systems with clock asynchronism: A signal processing perspective [special issue on signal processing for the integrated sensing and communications revolution],” *IEEE Signal Processing Magazine*, vol. 41, no. 5, pp. 31–43, 2024.
- [5] J. Zhao, Z. Lu, J. A. Zhang, S. Dong, and S. Zhou, “Multiple-target doppler frequency estimation in isac with clock asynchronism,” *IEEE Transactions on Vehicular Technology*, vol. 73, no. 1, pp. 1382–1387, 2024.
- [6] M. Canil, J. Pegoraro, J. O. Lacruz, M. Mezzavilla, M. Rossi, J. Widmer, and S. Rangan, “An experimental prototype for multistatic asynchronous isac,” ser. mmWave '23. New York, NY, USA: Association for Computing Machinery, 2023, p. 16–17. [Online]. Available: <https://doi.org/10.1145/3628357.3629710>
- [7] G. Ventura, Z. Bhalli, M. Rossi, and J. Pegoraro, “Bistatic doppler frequency estimation with asynchronous moving devices for integrated sensing and communications,” *IEEE Wireless Communications Letters*, 2024.
- [8] G. Ventura, M. Rossi, and J. Pegoraro, “Asymov: Integrated sensing and communications with asynchronous moving devices,” 2025. [Online]. Available: <https://arxiv.org/abs/2412.10387>
- [9] D. Philip Venmani, Y. Lagadec, O. Lemoult, and F. Deletre, “Phase and Time Synchronization for 5G C-RAN: Requirements, Design Challenges and Recent Advances in Standardization,” *EAI Endorsed Transactions on Industrial Networks and Intelligent Systems*, vol. 5, no. 15, p. e3, Aug. 2018. [Online]. Available: <https://publications.eai.eu/index.php/inis/article/view/401>
- [10] Ericsson, “Ericsson Cloud RAN,” Stockholm, Sweden, 2025, accessed: 2026-01-20. [Online]. Available: <https://www.ericsson.com/en/ran/cloud>
- [11] 3rd Generation Partnership Project, “3GPP TR 38.901 version 16.1.0 Release 16,” 2020. [Online]. Available: https://www.etsi.org/deliver/etsi_tr/138900_138999/138901/16.01.00_60/tr_138901v160100p.pdf
- [12] J. G. Proakis and D. G. Manolakis, *Digital signal processing (3rd ed.): principles, algorithms, and applications*. USA: Prentice-Hall, Inc., 1996.
- [13] J. Li and P. Stoica, *MIMO radar signal processing*. John Wiley & Sons, 2008.
- [14] The MathWorks, Inc., “5G Toolbox (R2023b),” [Computer software], Natick, Massachusetts, United States, 2023. [Online]. Available: <https://www.mathworks.com/products/5g.html>
- [15] 3rd Generation Partnership Project, “3GPP TS 38.101-1 version 18.6.0 Release 17,” 2024. [Online]. Available: https://www.etsi.org/deliver/etsi_ts/138100_138199/138101/18.06.00_60/ts_138101v180600p.pdf
- [16] J.-J. van de Beek, O. Edfors, M. Sandell, S. Wilson, and P. Borjesson, “On channel estimation in ofdm systems,” in *1995 IEEE 45th Vehicular Technology Conference. Countdown to the Wireless Twenty-First Century*, vol. 2, 1995, pp. 815–819 vol.2.